Advances in Civil Engineering

WILEY

RESEARCH ARTICLE OPEN ACCESS

Study on Seismic Performance of Precast Hollow Wall Panel Connected by Embedded Steel Box Joints

Yi Wang[1,2] | Yansong Li[2] | Xiangming Zhou[3] | Songzhao Qu[1] | Peibo You[1]

[1]School of Civil and Transportation Engineering, Henan University of Urban Construction, Pingdingshan 467036, Henan, China | [2]School of Civil Engineering and Architecture, China Three Gorges University, Yichang 443000, Hubei, China | [3]Department of Civil and Environmental Engineering, Brunel University of London, Middlesex, Uxbridge, UB8 3PH, UK

Correspondence: Yi Wang (wangy@huuc.edu.cn)

Received: 27 February 2025 | **Revised:** 6 April 2026 | **Accepted:** 5 June 2026

Academic Editor: Shikha Binwal

Keywords: aspect ratio | joint connection | precast hollow slab | ratio of axial compressive force to ultimate capacity | seismic performance | steel frame structure

ABSTRACT

In recent years, the advancement of modular prefabricated construction has driven the adoption of prefabricated hollow wall structures because of their lightweight and high strength characteristics. However, these structures face challenges, such as connection integrity, cohesion, and ease of assembly. To address these shortcomings, this study proposes an innovative prefabricated hollow wall structure featuring a novel joint connection system. A combination of experimental validation and finite element simulation was employed to assess the reliability of the new joint configuration as a load-bearing wall through nonlinear analysis. A subsequent parametric study evaluated the influence of factors such as the ratio of axial compressive force to ultimate capacity ratio, aspect ratio, and steel box dimensions on structural performance. The findings reveal that incorporating box-type joint connections significantly enhances the seismic resilience of prefabricated hollow wall structures. Increasing the aspect ratio leads to increase in yield load, ultimate bearing capacity, and structural ductility. Conversely, increasing the ratio of axial compressive force to ultimate capacity initially improves ultimate bearing capacity and yield strength before leading to a decline at higher ratios. Variations in ductility coefficients are also observed under different ratios of axial compressive force to axial compressive ultimate capacity ratios for hollow wall panels. Additionally, changes in steel box size also affect the structural load-carrying capacity, highlighting the importance of selecting appropriate dimensions for optimal assembly performance.

1 | Introduction

In recent years, prefabricated structures have garnered significant attention and widespread application both domestically and internationally due to their advantages, such as a comprehensive industrial chain, high construction efficiency [1, 2], excellent load-bearing capacity, and environmental sustainability. Rettinger et al. [3] and Gao et al. [4] have systematically reviewed the research on prefabricated structures in areas, including manufacturing processes, assembly technologies, cost control, and regulatory standards. In response to the State Council's "Opinions on Promoting Green Development of Urban and Rural Construction" [5], which underscores the importance of prefabricated housing construction, this study highlights the urgent need to enhance the standardization of components and improve the industrial chain to better address the living conditions of rural populations. This research innovatively transforms the traditional prefabricated residential structure, composed of

Yi Wang (1983), male, from Pingdingshan, Henan Province, Ph.D., Professor, Master's supervisor, is mainly engaged in the research of assembled new structures and their durability.

prefabricated panels and edge components, into a fully integrated prefabricated hollow panel system. Specifically, prefabricated hollow panels are arranged vertically as walls and horizontally as floors. This structural improvement not only effectively addresses the challenges associated with traditional prefabricated construction, such as complex construction procedures and excessive concrete usage, but also significantly enhances construction efficiency while conserving substantial human, material, and financial resources. Therefore, the application research of prefabricated hollow slabs as vertical load-bearing walls holds important theoretical value and practical significance.

Researchers around the world have extensively studied precast hollow wall structures and have made significant findings. Meng [6] experimentally demonstrated that precast concrete hollow walls have high axial compressive strength and stability in both vertical and out-of-plane displacements. Leigang [7] conducted low cyclic loading tests on precast concrete hollow slab shear walls and found that the specimens consistently exhibited compressive flexural failure, highlighting their overall robust performance. Chen et al. [8] further confirmed the excellent seismic performance of precast bidirectional hollow slab shear walls through similar tests. Zhang et al. [9] also emphasized the superior seismic performance of precast hollow core shear walls, noting that the diameter of the transversely inserted reinforcement had a minimal effect on this performance. The aforementioned studies show that precast hollow wall structures have good seismic performance. However, the existing studies mainly focus on small-sized precast hollow walls cast in special molds, which require a large number of splices to form the overall structure, and the quality of the splices can be found from the beam-column connections [10] to directly affect the overall performance of the structure. In prefabricated buildings, the connection between components is critical to ensure structural integrity and safety [11]. Current methods for horizontal connections between precast members and foundations include grouted sleeve connections [12, 13], grouted anchor connections [14, 15], and other innovative techniques [16–19], while vertical connections typically rely on connectors [20, 21]. These methods often face challenges such as difficult positioning, high costs, and inconsistent construction quality. For low-rise or multistory buildings, studies [22, 23] suggest that the separation of the lower part of precast panels and the use of restraint elements can achieve effective connections. In addition, as global energy efficiency standards for buildings continue to rise, precast hollow core panels are gaining popularity due to their superior thermal insulation properties [24, 25]. Research also indicates that these panels can serve as primary structural members [26, 27] and often exhibit progressive damage characteristics, providing a valuable theoretical basis for their practical application in engineering.

Our research group [28] has previously conducted experimental studies on the seismic performance of prefabricated hollow wall structures connected by double steel boxes under low-cycle reversed loading. To overcome the limitations of traditional prefabricated hollow walls, such as restricted mold size, poor integrity, and difficulty in connection, this study, based on the previous work, further proposes a new prefabricated wall structure system connected by single steel boxes. This system uses prefabricated hollow slabs as load-bearing walls, which have the advantage of a complete industrial chain. In theory, hollow slabs of any length can be fabricated, and they can be cut to the required length for independent structural units according to the actual engineering needs. This study focuses on the mechanical behavior of a single wall panel under low-cycle reversed loading, systematically investigating the influence of key parameters such as height-to-width ratio, axial compression ratio, and steel box size on seismic performance to verify the applicability of a single steel box connection in prefabricated hollow wall slabs. Meanwhile, to address the key issue of wall connection, this study

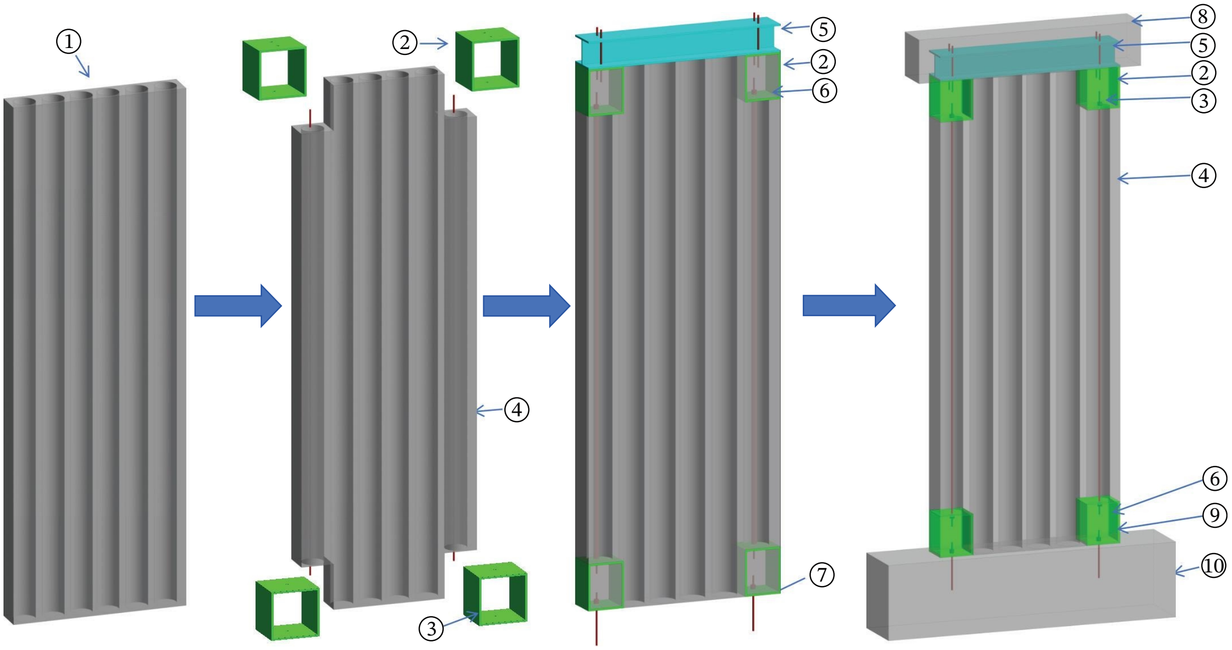

FIGURE 1 | Joint connection scheme. ① Prefabricated hollow plate, ② steel box, ③ jack reinforcement, ④ prefabricated hollow plate after cutting, ⑤ steel beam, ⑥ concrete filling box, ⑦ bolts, ⑧ loading beams, ⑨ steel box, and ⑩ ground beams.

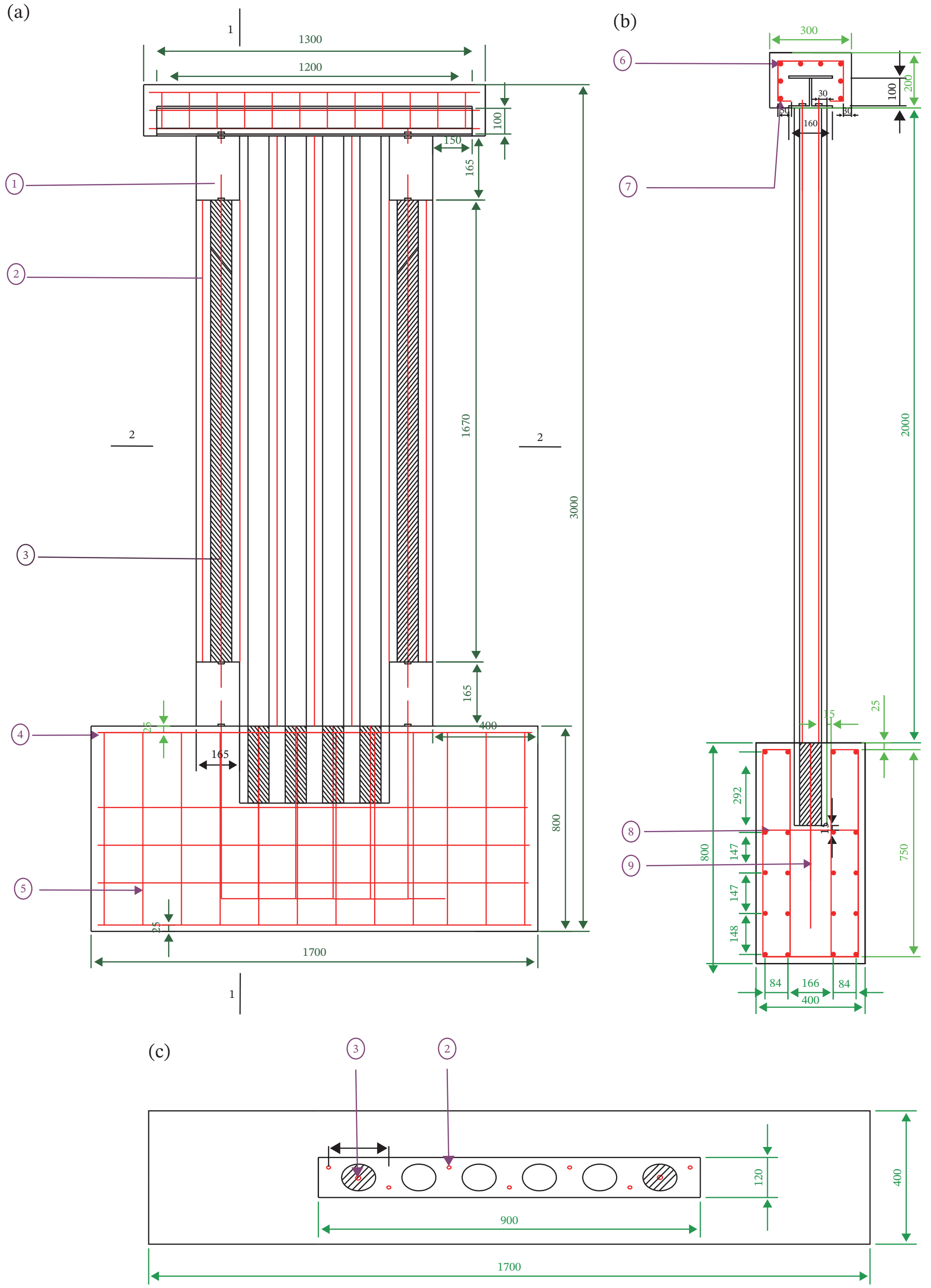

FIGURE 2 | Hollow slab wall diagram. (a) front view, (b) 1–1 profile, and (c) section 2–2. ① Perforated reinforcement C12, ② internal reinforcement C9.3@142, ③ Concrete pouring hole C12, ④ transverse rib 20C16, ⑤ hooped reinforcement C8@150, ⑥ transverse rib 20C16, ⑦ hooped reinforcement C8@150, ⑧ hooped reinforcement C8@150, and ⑨ anchored reinforcement C12.

innovatively proposes a new type of node connection method, which forms a complete wall structure system through a standardized node assembly. This connection method not only significantly improves the convenience of wall connection but also effectively enhances the integrity and reliability of the structure, providing a theoretical basis and data support for the subsequent development of green prefabricated rural housing structure systems.

2 | A Novel Joint Connection

This study introduces a novel joint connection system for prefabricated hollow slab wall structures. The system begins with the fabrication of a cuboid steel member without front and back steel covers. Four square slots were cut at the corners of the hollow wall panel to fit the steel member's dimensions. Grouting is then applied to the panel's left and right holes, embedding

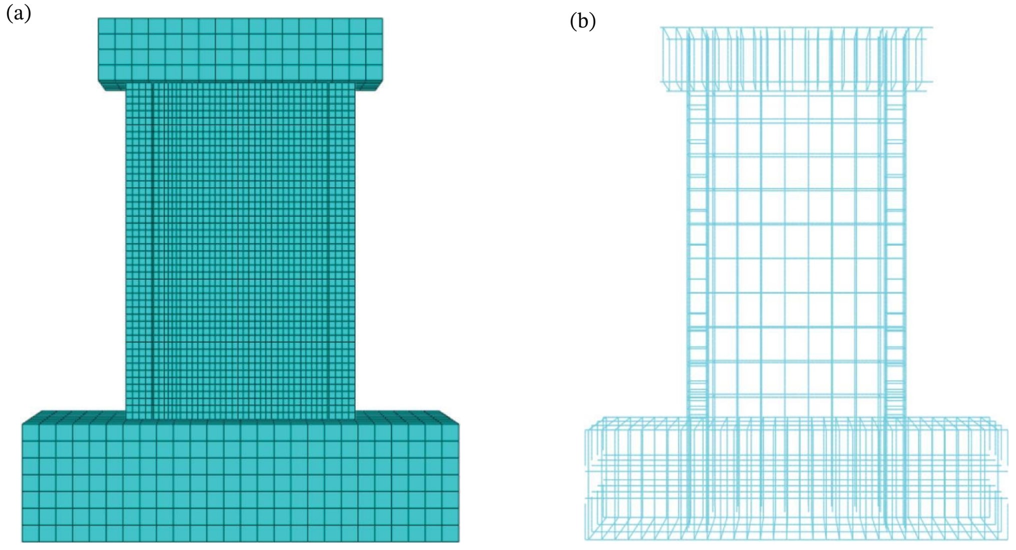

FIGURE 3 | Meshing of the specimen model. (a) Overall grid model. (b) Rebar grid model.

threaded perforated steel bars with exposed ends for secure connections. Steel connectors are placed within each slot. For the upper connectors, central holes in their bottom surfaces allow the bolts to connect the exposed threaded steel bars. Additional holes on their top surfaces facilitate connections to a supporting steel beam. Similarly, lower connectors are bolted to the threaded steel bars at the top and bottom surfaces, securing connections to the upper floor beam. Finally, grout is applied within each steel connector, and steel covers are welded to form a unified structure (Figure 1).

The steel box used in this study has dimensions of 165 mm (length) × 165 mm (width) × 120 mm (height), with a wall thickness of 10 mm. The steel box is connected to the wall structure by four M20 high-strength bolts, with the bolt preload determined in accordance with the "Code for Design of Steel Structures" (GB 50017-2017). In the finite element modeling, the contact between the bolts and the steel plate is modeled using a "constraint" condition, assuming no relative slippage between the two during loading; this assumption is reasonable provided that the bolt preload is sufficient and no yielding has occurred.

TABLE 1 | Concrete properties.

Specimen number	Design compressive strength, f_c (MPa)	Cubic compressive strength, f_{cu} (MPa)	Tensile strength f_{tk} (MPa)	Elastic modulus E_c ($\times 10^4$ MPa)	Poisson ratio μ
WA4-2	60	52.47	2.85	3.60	0.2
WC4-2		50.82			

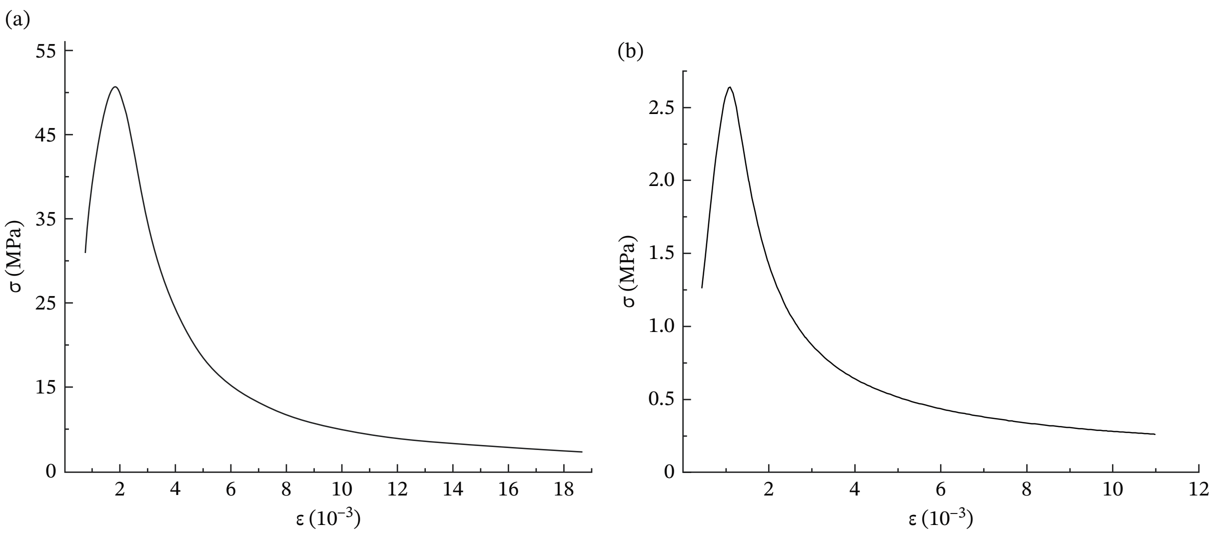

FIGURE 4 | Constitutive law of concrete. (a) Compression stress–strain curve. (b) Tensile stress–strain curve.

In this test, the precast hollow-core slab walls were constructed using C60 concrete, with Grade 1860 prestressed steel strands embedded within the walls and arranged in a staggered reinforcement pattern with a tension coefficient of 0.35. The voids were filled with 12 mm diameter HRB400 reinforcing bars. CBGM-300 high-strength nonshrink grout was used in the joint areas; tested in accordance with the GB/T 50448-2015 standard, its compressive strength at 28 days was 61.9 MPa. Q345 steel was selected for the structural steelwork.

In the study, three main types of concrete elements are included, which are precast hollow core slabs, floor beams, and loading beams (built-in I-beams). The hollow core slab wall dimensions and reinforcement are shown in Figure 2.

3 | Model Verification

3.1 | Specimen Parameters

The finite element modeling framework employed in this chapter (including the types of elements, contact definitions, boundary conditions, and loading schemes) is based on [28], where the accuracy of this method was systematically verified. Accordingly, this paper adopts the modeling parameters from [28] without repeating the verification. However, the validation objects here are two specimens (WA4-2 and WC4-2) from [29]. Therefore, finite element models were independently established for these two specimens. All material constitutive models, mesh sizes, and contact parameters presented later were independently determined based on convergence analysis of the current models, rather than directly taken from [28]. To verify the accuracy of the finite element parameters, specimens WA4-2 and WC4-2 from [29] were selected as verification models. Their parameters are as follows: overall height 2090 mm, loading beam section 420 mm × 350 mm (length 1730 mm), and ground beam section 750 mm × 650 mm (length 2600 mm).

3.2 | Establishment of Finite Element Model

3.2.1 | Mesh Size Determination and Element Assignment

In the finite element software ABAQUS, a three-dimensional truss element (T3D2) was used for simulating reinforcement, while a three-dimensional eight-joint solid element with linear reduced integration (i.e., C3D8R) was used for modeling concrete. The mesh size was set to 50 mm for concrete, 250 mm for loading and ground beams, and 50 mm for steel reinforcement, as shown in Figure 3.

To verify the effect of mesh size on the calculation results, simulations were performed on the WA4-2 specimen using three mesh sizes: 30, 50, and 80 mm. The results show that the difference in ultimate load-bearing capacity between the 30 and 50 mm meshes was less than 2%, whilst the error for the 80 mm mesh reached 8.6%. Taking into account both computational efficiency and accuracy, this study employs a 50 mm mesh for concrete members, a 50 mm mesh for the reinforcement, and a 250 mm mesh for beam and column members.

3.2.2 | Material Constitutive Laws

Material constitutive laws significantly affect the numerical simulation accuracy. ABAQUS employs a tensile plastic damage model suitable for concrete structures. Based on specimen design data from [29] and the Chinese National Code for Design of Concrete Structures (GB 50010-2010) [30], the properties of concrete are detailed in Table 1, and the uniaxial stress–strain relationship of concrete is illustrated in Figure 4.

The parameters for the concrete damage plasticity (CDP) model are set as follows: the expansion angle is taken as 30°, the eccentricity as 0.1, the ratio of biaxial compressive strength to uniaxial compressive strength as 1.16, the ratio of the second stress invariant in the tensile meridian to that in the compressive meridian as 0.6667, and the viscosity coefficient as 0.005. This parameter system was calibrated and determined based on GB 50010-2010 and experimental data from [29]. The overall modeling approach follows our previous work [28], but the specific parameters (e.g., concrete strength and steel yield strength) are based on the material tests of specimens WA4-2 and WC4-2 in [29].

For reinforcement, a bi-linear stress–strain model was used (Figure 5), with properties derived from the Chinese National Code for Design of Steel Structures (GB50017-2017) [31], as listed in Table 2.

3.2.3 | Contact, Boundary Conditions, and Loading Methods

The steel plate within the hollow slab wall was fully embedded into the concrete, assuming perfect bonding without any slip. Similarly, the connection between the bolt and the steel plate was modeled as fully intact. The bottom beam was fixed, while the top loading beam was constrained to move only along the plane of the wall.

The loading process was divided into two stages:

1. Vertical load: This simulated both constant and live loads, applied as a concentrated force at the central coupling point on the top surface of the loading beam.

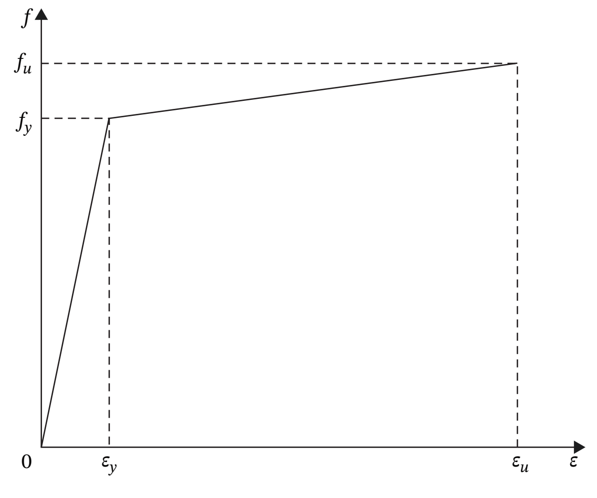

FIGURE 5 | Stress–strain relationship of steel bar.

TABLE 2 | Steel properties.

Brand	Diameter (mm)	Yield strength f_y (MPa)	Tensile strength f_u (MPa)	Elongation (%)	Elastic modulus E_s ($\times10^5$ MPa)	Poisson ratio μ
HPB300	6	300	420	19	2.10	0.3
HRB400	8	448	652		2.23	
	10	458	666		2.10	

2. Horizontal cyclic load: The amplitude of this load was determined using force–displacement control, following the guidelines of JGJ/T101-2015 [32]. It was applied at the end cross-section of the loading beam until structural failure occurred.

Based on these conditions, a finite element model of the hollow slab wall was developed. As shown in Figure 6.

This test was conducted in accordance with the JGJ/T 101-2015 standard, employing a force–displacement control method for loading. The failure criteria strictly adhered to the provisions of this standard, with failure of the test specimen determined by meeting any one of the following conditions: (1) the horizontal load drops to 85% of the peak load and (2) the displacement angle reaches 1/50. All specimens were assessed for failure using a uniform standard, ensuring the comparability of the test results and consistency in the evaluation.

3.3 | Verification of Finite Element Model

Finite element models FEM-1 and FEM-2, corresponding to specimens WA4-2 and WC4-2 in the literature, were established.

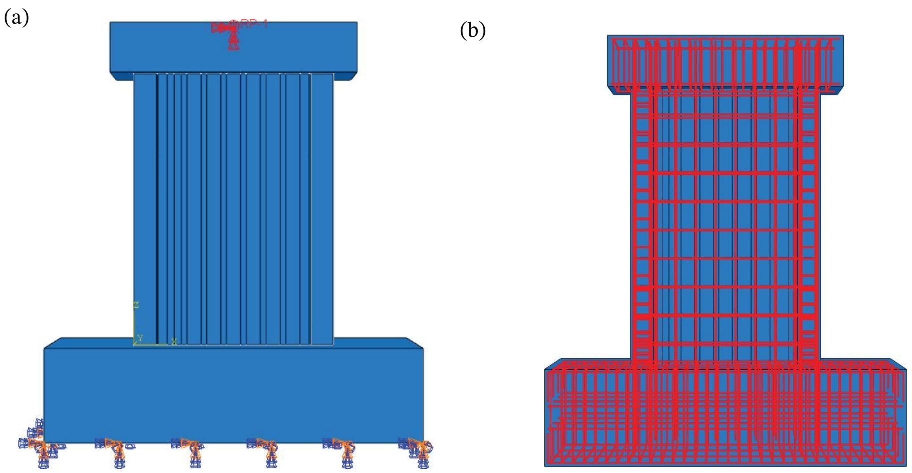

FIGURE 6 | ABAQUS model diagram. (a) Model boundary conditions. (b) The steel bars are embedded within the concrete.

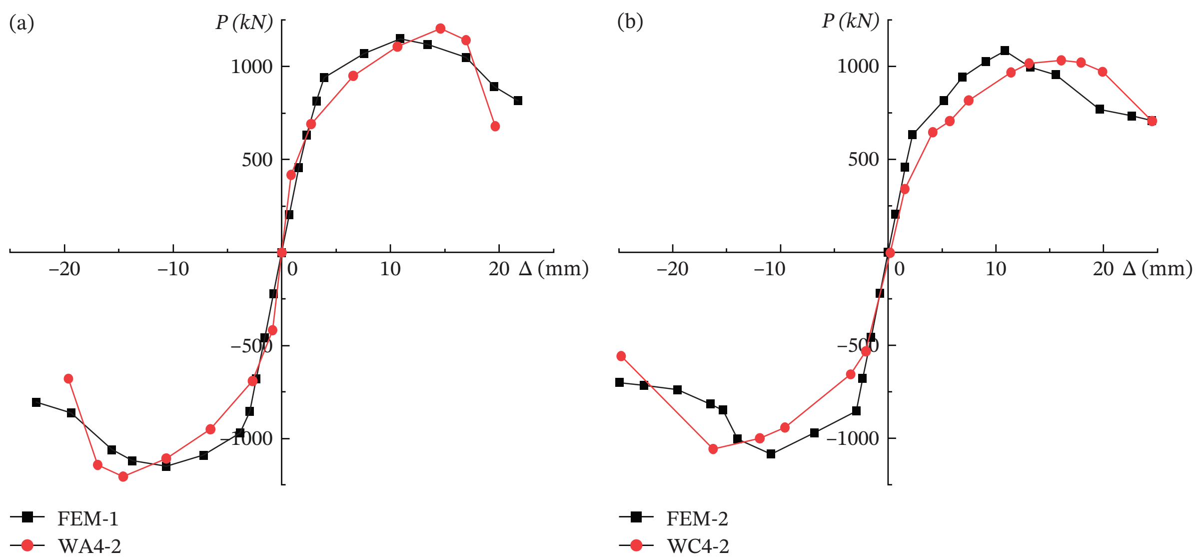

FIGURE 7 | Comparison of skeleton curves between test specimens and finite element specimens. (a) WA4-2 and FEM-1 skeleton curves. (b) WC4-2 and FEM-2 skeleton curves.

TABLE 3 | Simulated vs. experimental ultimate load bearing capacity.

Peer group	Specimen number	Ultimate bearing capacity, *P* (kN)	Relative error
1	FEM-1	1150	−4.5%
	WA4-2	1205	
2	FEM-2	1085	+3.8%
	WC4-2	1045	

TABLE 4 | Information of aspect ratio dimensions.

Specimen number	AHSW-1	AHSW-2
Steel box size	Nil	165 mm × 165 mm×120 mm

Skeleton curves from simulation and experiments were compared (Figure 7).

Figure 7a,b and Table 3 show strong agreement between experimental and numerical skeleton curves. Initially, specimens displayed stable lateral stiffness, which progressively decreased with

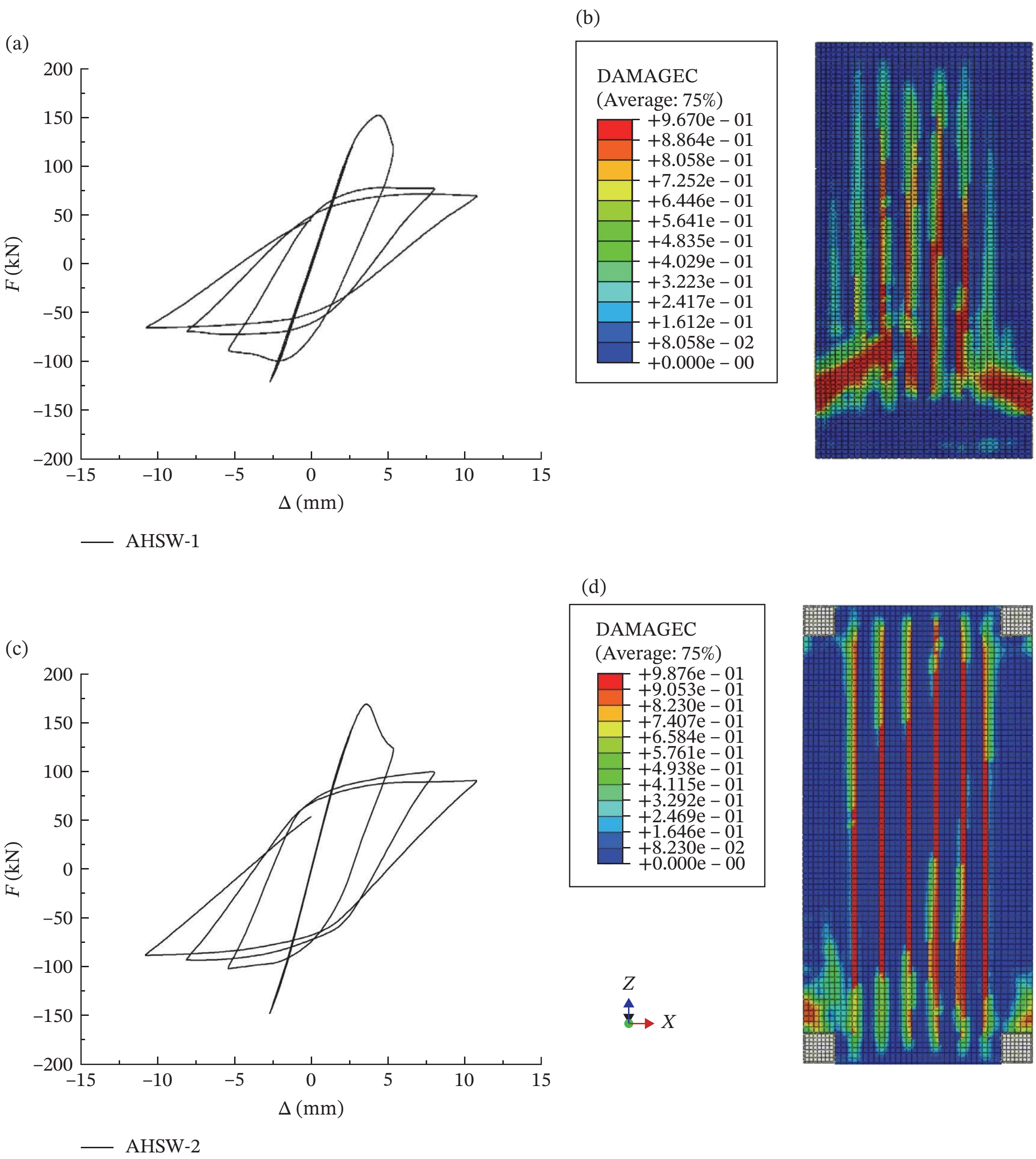

FIGURE 8 | Hysteresis curve and wall failure pattern. (a) The restoring force characteristic curve of specimen AHSW-1. (b) Specimen AHSW-1 failure pattern diagram. (c) The restoring force characteristic curve of specimen AHSW-2. (d) Specimen AHSW-2 failure pattern diagram.

increasing load due to concrete damage, as indicated by the skeleton curve slope. The peak error between experimental and simulated results was less than 5%, confirming the feasibility and accuracy of the finite element parameters and models.

4 | Comparative Study of Joint Connections

Based on the aforementioned material principal structure and modeling methodology, the following model is constructed. When setting up the interactions for the model in this test, it was assumed that there was good restraint between the concrete and the steel plates and reinforcing bars, and any bond slip between the materials was neglected. The embedded command was used to place the steel plates and reinforcing bars within the concrete. At the same time, it was assumed that the bolts and connectors were securely fastened, and any slip between them was neglected; a "constraint" was used to simulate the contact between them. All contacts within the concrete were simulated using constraints. For rigid connection components, face-to-face contact is employed between contact surfaces. In the normal direction, both contact and separation between steel plates are permitted, and this is simulated using "hard contact." In the tangential direction, slight relative displacement and force transfer between contact surfaces are allowed, and this is simulated using "Coulomb friction," with the friction coefficient set to 0.6 [33]. When performing finite element analysis, to apply prestressing, the expansion coefficient must first be added to the reinforcement properties. Subsequently, a predefined temperature field is created in the load function, and the prestressing requirements are met by varying the temperature. The load is simulated by applying a downward displacement; this is achieved by applying a downward vertical displacement at the central coupling point on the top surface of the slab, thereby ensuring consistency with the test.

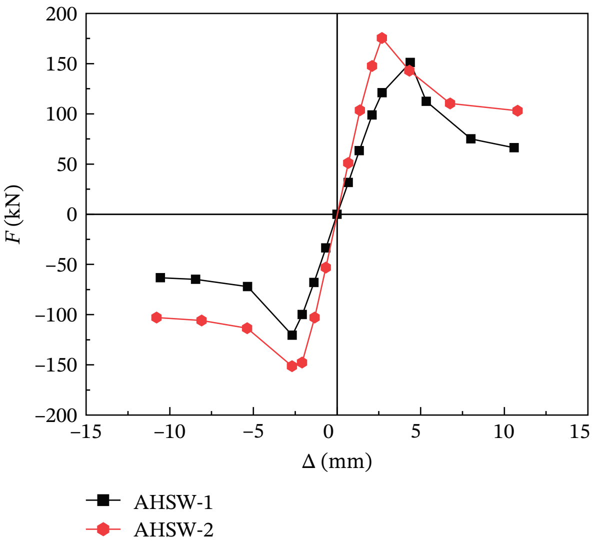

FIGURE 9 | Comparison of skeleton curves.

TABLE 5 | Yield and ultimate loads from experiment.

Specimen number	Direction	P_y (kN)	$P_{\bar{y}}$ (kN)	P_u (kN)	$P_{\bar{u}}$ (kN)
AHSW-1	Ortho	138.3	127.1	151.2	135.9
	Minus	115.8		120.6	
AHSW-2	Ortho	156.7	149.3	169.3	158.6
	Minus	141.9		147.8	

Finite element models, AHSW-1 and AHSW-2, were developed to compare the performance of prefabricated hollow panel walls under two connection methods. AHSW-1 utilized conventional concrete pouring (failure to cut wall corners and set into steel box), while AHSW-2 employed the proposed connection method (Table 4). Comparative analyses included hysteretic curves, skeleton curves, stiffness, ductility, and energy dissipation.

4.1 | Hysteresis Curve and Cloud Map Analysis

Under identical cyclic loading, AHSW-2 exhibited fuller hysteretic curves with larger enclosed areas compared to AHSW-1 (Figure 8), indicating superior energy dissipation and seismic performance. It can be clearly seen from the damage maps that the two corners of the floor of sample AHSW-1 were severely damaged; in contrast, sample AHSW-2 was optimized by cutting the two corners of the floor and assembling a steel box, which effectively improved the stiffness of the floor and thus significantly reduced the degree of damage to the floor of the wall. In addition, the damage in the center of both specimens was concentrated in the vicinity of the holes, which is highly consistent with the typical damage pattern of precast hollow walls, further confirming the reliability of the test results.

4.2 | Skeleton and Bearing Capacity Analysis

As shown in Figure 9 and Table 5, the skeleton curve of AHSW-2 displayed slower stiffness degradation and smaller lateral displacement under similar damage conditions. AHSW-2 also demonstrated a higher ultimate bearing capacity and yield strength than AHSW-1, confirming the effectiveness of the proposed connection method.

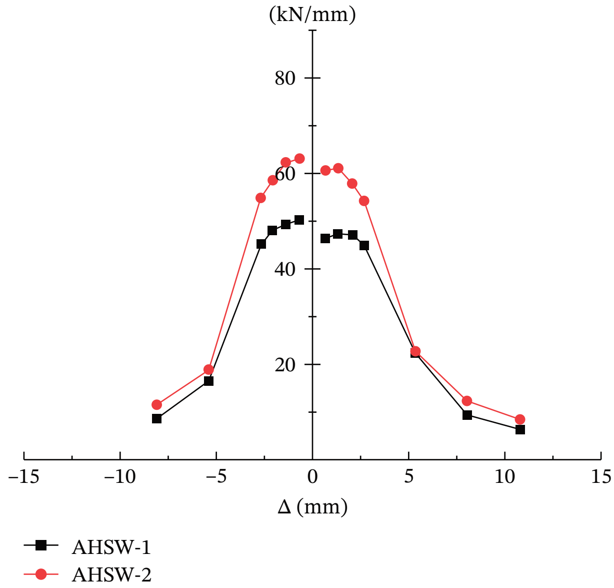

FIGURE 10 | Comparison of stiffness degradation.

TABLE 6 | Displacement angle of specimens.

Specimen number	Yield		Peak value		Limit		Ductility coefficient
	Displacement (mm)	Displacement angle (rad)	Displacement (mm)	Displacement angle (rad)	Displacement (mm)	Displacement angle (rad)	
AHSW-1	3.10	1/800.00	7.22	1/343.49	4.31	1/575.41	1.40
AHSW-2	2.84	1/873.24	10.74	1/230.92	4.61	1/537.70	1.63

4.3 | Lateral Stiffness and Ductility Analysis

Figure 10 shows that AHSW-2 experienced slower stiffness degradation than AHSW-1, confirming the reliability of the proposed connection. Additionally, Table 6 highlights AHSW-2's smaller displacement angle at the yield stage, signifying improved ductility.

The displacement angle is calculated as shown in Equation (1).

$$\theta = \frac{\Delta}{H}, \tag{1}$$

where Δ is the wall vertex displacement; H is the wall height; and θ is the displacement angle.

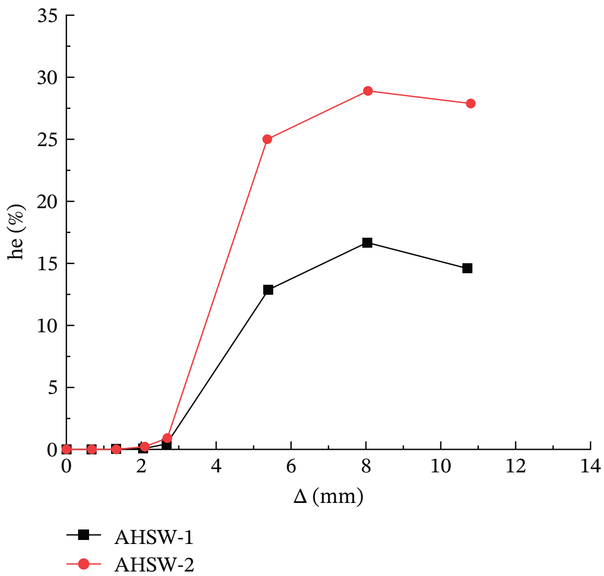

FIGURE 11 | Comparison of equivalent viscous damping coefficients.

4.4 | Energy Consumption Capacity

Figure 11 illustrates that both AHSW-1 and AHSW-2 exhibited increasing equivalent viscous damping coefficients (he) with horizontal displacement, peaking at the ultimate load. However, AHSW-2 showed improved hysteretic fullness, bearing capacity, and ductility.

In summary, AHSW-2, the connection mode proposed herein, demonstrates superior performance in hysteretic behavior, bearing capacity, stiffness degradation, ductility, and energy consumption compared to AHSW-1. These findings validate the reliability of the new connection mode. Further parametric analyses based on AHSW-2 evaluated the influence of the aspect ratio and axial compressive force ratios on performance.

4.5 | Changes in Damage to Steel Boxes

As shown in Figure 12, stress concentration in this steel frame occurs only locally at the reinforcement joints connecting the bottom, top, loading beam, and ground beam, with overall damage remaining minimal. This distribution pattern significantly mitigates the vulnerability inherent in the original wall's base. Simultaneously, stresses across all regions of the steel box remain consistently below their yield strength. This prevents plastic deformation while enabling the structure to stably bear and distribute loads through its self-constraint and force-transfer mechanisms. This capability is precisely the core reason for its enhanced structural performance. Throughout the entire cyclic loading process, the stress history of the upper and lower steel boxes was monitored. The results indicate that even at peak load, the maximum stress in the steel boxes remained below the yield strength of Q345 steel (345 MPa), and none of the joints entered the plastic stage. Stress concentrations were observed only around the bolt holes, and the overall damage was minimal, demonstrating that the joint possesses good elastic recovery capacity and reliability under cyclic loading.

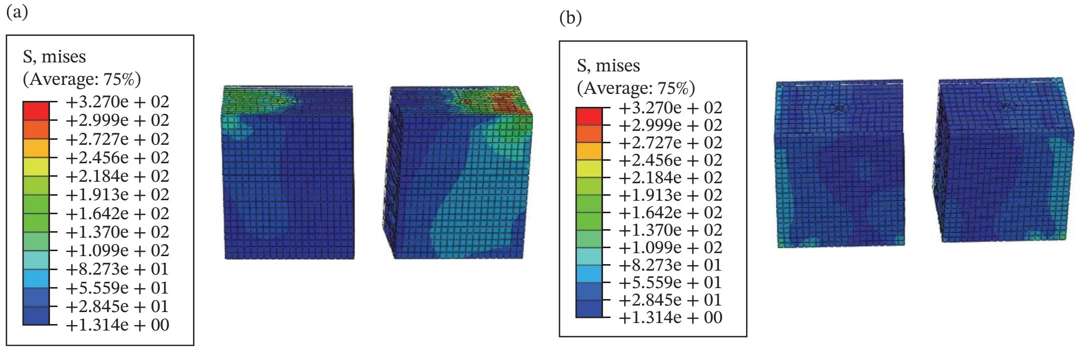

FIGURE 12 | Damage cloud map of steel components. (a) Upper steel box. (b) Lower steel box.

TABLE 7 | Dimensional details of the three specimens.

Specimen number	Aspect ratio	Wall width (mm)	Wall height (mm)
AHSW-A-1	1.87	1200	2250
AHSW-A-2	2.07		2480
AHSW-A-3	2.17		2600

5 | Parametric Study

5.1 | Aspect Ratio

Finite element analysis was conducted under conditions where other parameters remained unchanged for three aspect ratios: 1.87, 2.07, and 2.17. Comparative analyses were performed on skeleton curves, stiffness curves, and displacement angles. Table 7 provides the dimensional details of the three specimens.

5.1.1 | Skeleton Curve and Bearing Capacity

Figure 13 and Table 8 illustrate the hysteresis plot, consistent skeleton curves, and damage patterns across the three specimens. As the aspect ratio increases, the ultimate bearing capacity of the structure decreases, accompanied by reduced stiffness and enhanced deformation capability. The skeleton curve's slope diminishes progressively, with greater stiffness and lower lateral displacement observed in undamaged walls. However, as damage intensifies, stiffness declines and lateral displacement increases. The initial stiffness shows a rapid decline, followed by a more gradual reduction.

5.1.2 | Lateral Stiffness and Ductility

Figure 14 reveals that as the aspect ratio increases, the initial stiffness of hollow slab wall structures decreases significantly. Specimen AHSW-A-1, with a smaller height-to-width ratio, exhibits reduced plasticity and increased brittleness, resulting in more pronounced stiffness degradation under lateral displacement. However, all specimens show comparable stiffness degradation upon reaching ultimate load capacity. Table 9 shows that AHSW-A-2 has the largest yield displacement, while AHSW-A-3 exhibits the highest ultimate displacement. Although the ductility coefficient is minimally affected by aspect ratio variations, AHSW-A-3 demonstrates superior ductility. However, its inadequate bearing capacity limits its applicability in practical engineering projects.

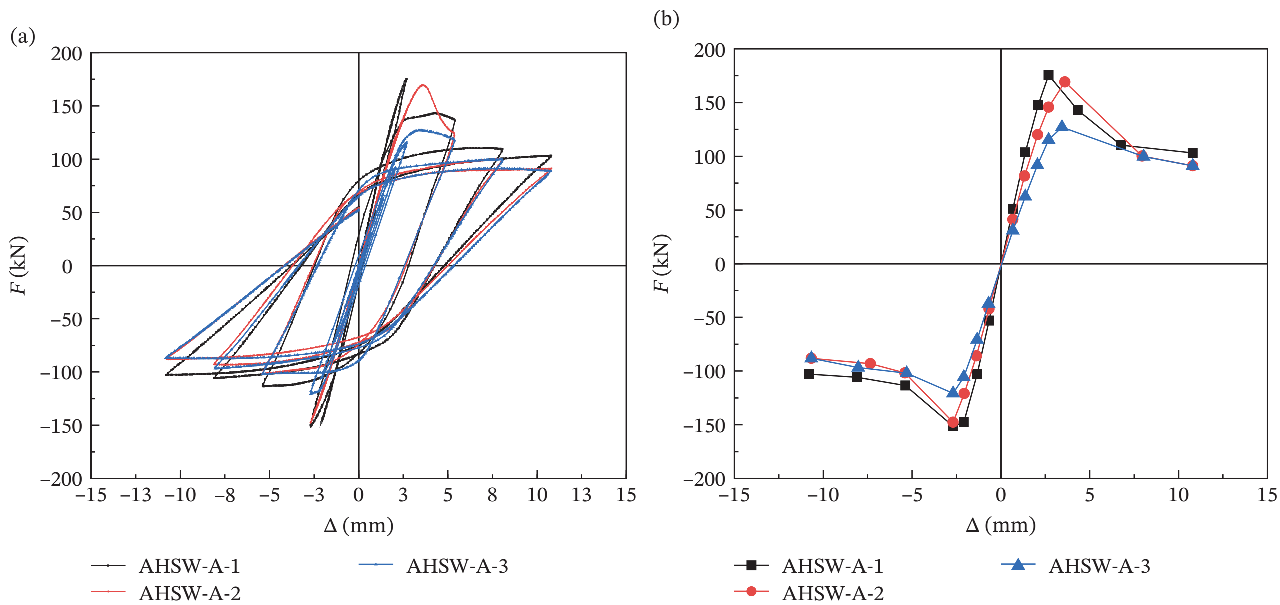

FIGURE 13 | The comparison chart of hysteresis and skeleton curves under different aspect ratios. (a) Hysteresis plot. (b) Skeleton curve.

TABLE 8 | Yield and ultimate loads from numerical analyses.

Specimen number	Direction	P_y (kN)	$P_{\bar{y}}$ (kN)	P_u (kN)	$P_{\bar{u}}$ (kN)
AHWS-A-1	Ortho	166.7	156.9	175.6	163.5
	Minus	147.1		151.3	
AHWS-A-2	Ortho	156.7	149.3	169.3	158.6
	Minus	141.9		147.8	
AHWS-A-3	Ortho	119.2	116.1	127.1	123.9
	Minus	113.0		120.7	

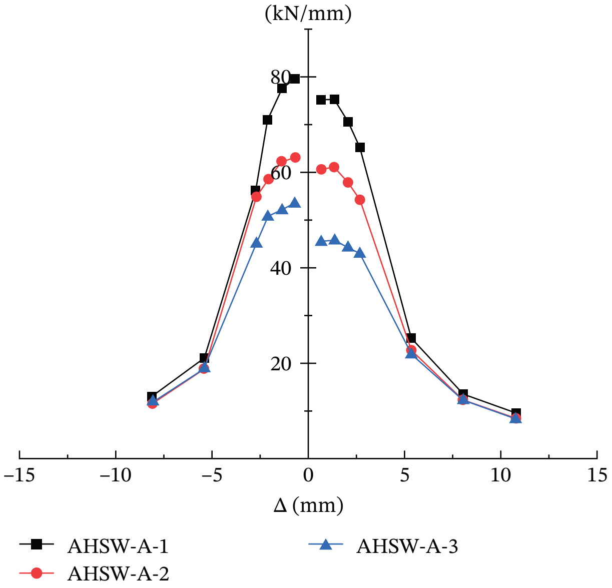

FIGURE 14 | Stiffness degradation curves of specimens AHSW-A-1–3.

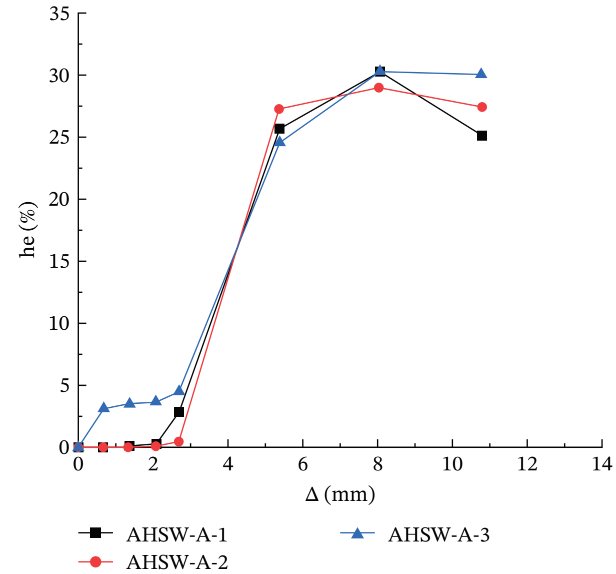

FIGURE 15 | Equivalent viscous damping coefficients of specimens AHSW-A-1–3.

Table 10 indicates no clear linear relationship between the aspect ratio and displacement angle. Nevertheless, the ultimate displacement angle increases with the wall's height.

5.1.3 | Energy Dissipation Capacity

Figure 15 highlights similar trends among the specimens' equivalent viscous damping coefficients. Initially, during horizontal loading, the specimens remain elastic, and energy dissipation is minimal. As displacement increases, the stiffness deteriorates, leading to higher damping coefficients and enhanced energy dissipation. Upon reaching ultimate load conditions, the damping coefficients decrease, signaling reduced seismic resistance.

Specimen AHSW-A-3, with its larger aspect ratio, demonstrates superior energy dissipation. However, its insufficient bearing capacity renders it unsuitable for practical applications.

5.2 | Ratio of Axial Compressive Force to Ultimate Capacity

Finite element analysis was performed on specimens with axial compressive force-to-ultimate capacity ratios of 0.3, 0.5, and 0.6. Comparative analyses were conducted on skeleton curves,

TABLE 9 | Ductility coefficients of specimens AHSW-A-1–3.

Specimen number	Direction	Δ_y (mm)	$\Delta_{\bar{y}}$ (mm)	Δ_u (mm)	$\Delta_{\bar{u}}$ (mm)	$\bar{\mu}$
AHSW-A-1	Ortho	2.51	2.30	4.02	4.16	1.81
	Minus	2.08		4.30		
AHSW-A-2	Ortho	3.12	2.84	5.21	4.61	1.63
	Minus	2.56		4.00		
AHSW-A-3	Ortho	2.92	2.65	6.65	5.94	2.25
	Minus	2.38		5.22		

TABLE 10 | Displacement angles of specimens AHSW-A-1–3.

	Yield		Peak value		Limit		
Specimen number	Displacement (mm)	Displacement angle (rad)	Displacement (mm)	Displacement angle (rad)	Displacement (mm)	Displacement angle (rad)	Ductility coefficient
AHSW-A-1	2.30	1/978.26	10.80	1/208.33	4.16	1/540.87	1.81
AHSW-A-2	2.84	1/873.24	10.74	1/230.92	4.61	1/537.70	1.63
AHSW-A-3	2.65	1/981.14	8.04	1/323.38	5.94	1/437.71	2.25

TABLE 11 | Ratios of axial compressive force to ultimate capacity of specimens AHSW-C-1–3.

Specimen number	Design ratio of axial compressive force to ultimate capacity	Design axial force (kN)
AHSW-C-1	0.3	921.7
AHSW-C-2	0.5	1536.1
AHSW-C-3	0.6	1843.3

stiffness curves, and displacement angles. Table 11 presents the ratios for the three specimens.

5.2.1 | Skeleton Curve and Bearing Capacity

Figure 16 and Table 12 reveal consistent skeleton curves and failure patterns among the specimens. However, when the ratio reaches 0.6, the prefabricated hollow panel wall experiences more severe damage; and AHSW-C-1 exhibits the largest deformation and energy dissipation capacity, AHSW-C-2 exhibits the smallest deformation and energy dissipation capacity, while AHSW-C-3 is in between.

5.2.2 | Lateral Stiffness and Ductility

Figure 17 demonstrates a significant decline in initial stiffness with increasing axial compressive force-to-ultimate capacity ratios. Stiffness degradation remains consistent across all specimens under horizontal loading.

Table 13 indicates that AHSW-C-1 has the highest yield and ultimate displacement, demonstrating superior ductility. A ratio of 0.3 is recommended for practical engineering applications due to its balance of ductility and bearing capacity.

Table 14 suggests that the displacement angle initially decreases with increasing ratios but begins to increase at higher values, reflecting complex interactions between structural forces.

5.2.3 | Energy Dissipation Capacity

Figure 18 shows that all specimens exhibit similar trends in their viscous damping coefficients. AHSW-C-3, with its higher axial pressure ratio, achieves better energy dissipation but suffers from insufficient bearing capacity, making it unsuitable for practical use.

Although the ultimate bearing capacity of AHSW-C-2 (axial compression ratio 0.5) is approximately 7.3% higher than that of

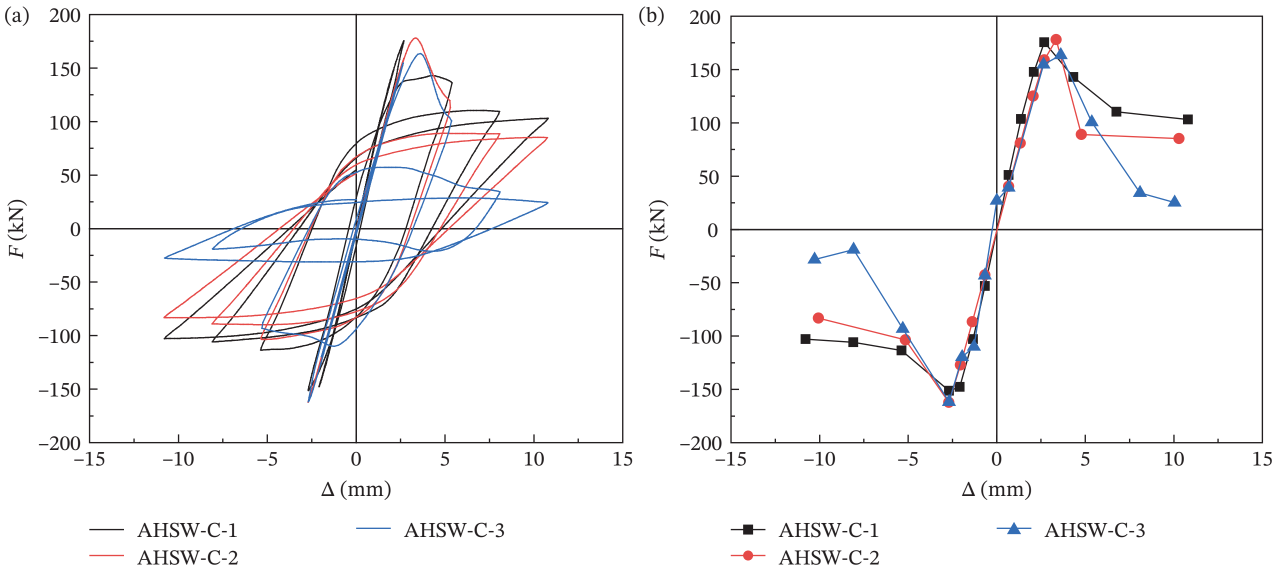

FIGURE 16 | The comparison chart of hysteresis and skeleton curves under different design ratio of axial compressive force to ultimate capacity. (a) Hysteresis plot. (b) Skeleton curve.

TABLE 12 | Yield and ultimate loads from experiments.

Specimen number	Direction	P_y (kN)	$P_{\bar{y}}$ (kN)	P_u (kN)	$P_{\bar{u}}$ (kN)
AHSW-C-1	Ortho	156.7	149.3	169.3	158.6
	Minus	141.9		147.8	
AHSW-C-2	Ortho	167.9	163.2	178.1	170.2
	Minus	159.1		162.2	
AHSW-C-3	Ortho	156.1	158.1	163.5	162.4
	Minus	160.0		161.2	

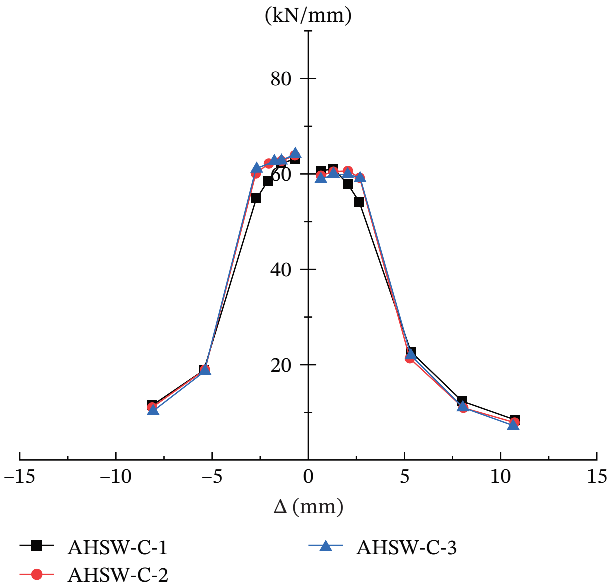

FIGURE 17 | Stiffness degradation of specimens AHSW-C-1–3.

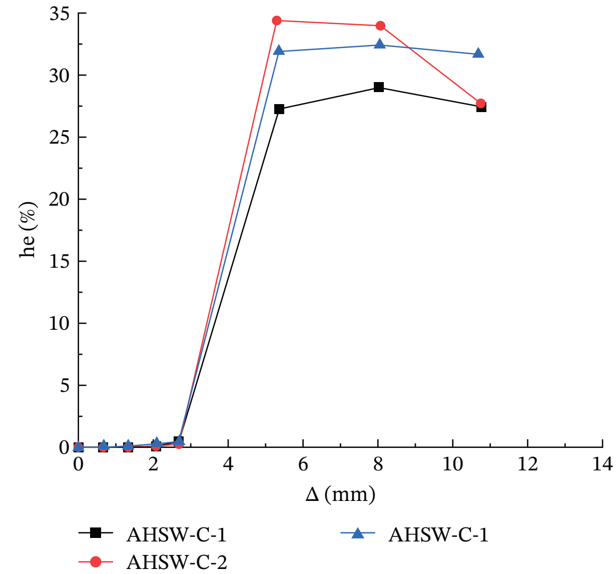

FIGURE 18 | Equivalent viscous damping coefficients of specimens AHSW-C-1–3.

AHSW-C-1 (axial compression ratio 0.3), its ductility coefficient decreases by 19%, and the equivalent viscous damping coefficient decays more rapidly after the peak load. Considering the seismic performance comprehensively, 0.3 axial compression ratio achieves a better balance among bearing capacity, ductility, and energy dissipation capacity, and therefore is recommended as the engineering value.

TABLE 15 | Dimensions of steel boxes in various specimens.

Specimen number	AHSW-D-1	AHSW-D-2	AHSW-D-3
Steel box	165 × 200 × 120	165 × 180 × 120	165 × 165 × 120

5.3 | Steel Box Dimensions

Finite element analysis was performed for steel box sizes of 165 mm × 165 mm × 120 mm and 165 mm × 200 mm × 120 mm. Skeleton curves, stiffness curves, and displacement angles were analyzed for comparative study. Table 15 provides the size information.

5.3.1 | Skeleton Curve and Bearing Capacity

Figure 19 shows an increase in the ultimate bearing capacity with larger steel box sizes. However, excessive size increases can negatively impact structural performance, underscoring the

TABLE 13 | Ductility coefficients of specimens AHSW-C-1–3.

Specimen number	Direction	Δ_y (mm)	$\Delta_{\bar{y}}$ (mm)	Δ_u (mm)	$\Delta_{\bar{u}}$ (mm)	$\bar{\mu}$
AHSW-C-1	Ortho	3.12	2.84	5.21	4.61	1.63
	Minus	2.56		4.00		
AHSW-C-2	Ortho	3.00	2.82	3.79	3.75	1.32
	Minus	2.64		3.71		
AHSW-C-3	Ortho	2.80	2.73	4.61	4.11	1.51
	Minus	2.66		3.61		

TABLE 14 | Displacement angles of specimens AHSW-C-1–3.

	Yield		Peak value		Limit		
Specimen number	Displacement (mm)	Displacement angle (rad)	Displacement (mm)	Displacement angle (rad)	Displacement (mm)	Displacement angle (rad)	Ductility coefficient
AHSW-C-1	2.84	1/873.24	10.74	1/230.92	4.61	1/537.70	1.63
AHSW-C-2	2.82	1/873.24	10.07	1/246.28	3.75	1/661.34	1.32
AHSW-C-3	2.73	1/981.14	10.12	1/245.06	4.11	1/603.41	1.51

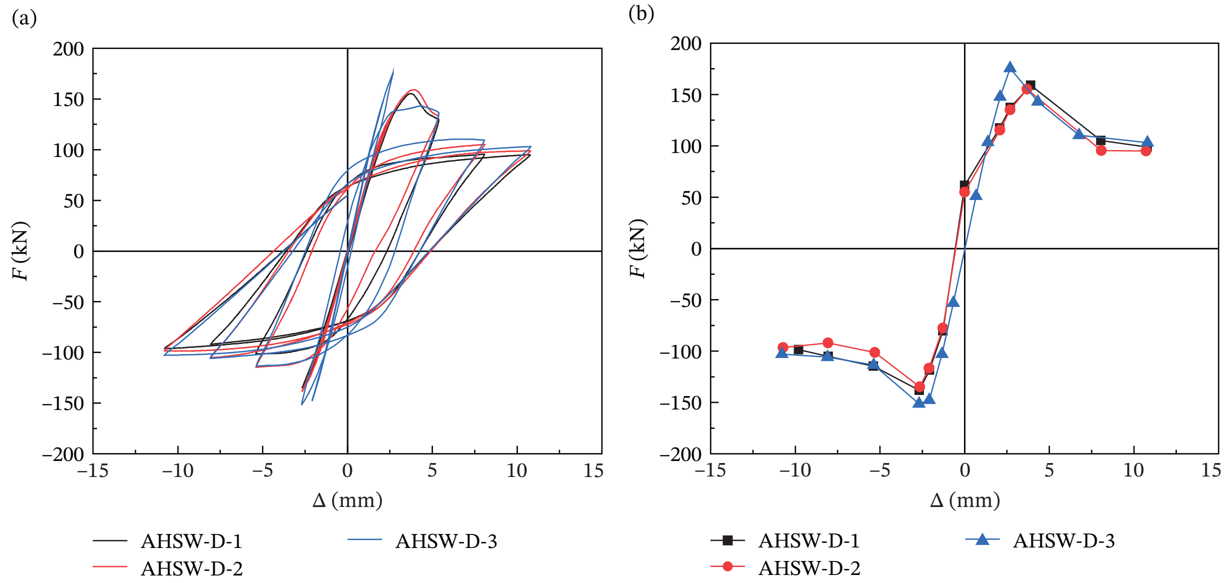

FIGURE 19 | The comparison chart of hysteresis and frame curves under different steel box dimensions. (a) Hysteresis plot. (b) Skeleton curve.

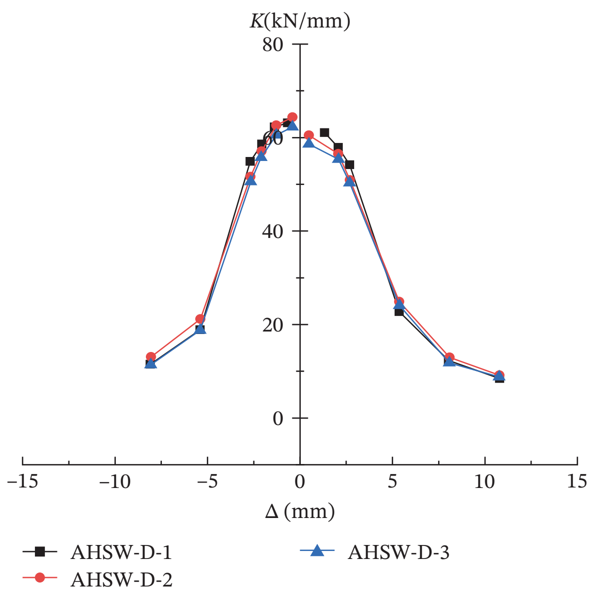

FIGURE 20 | Comparison of lateral stiffness of AHSW-D-1–3.

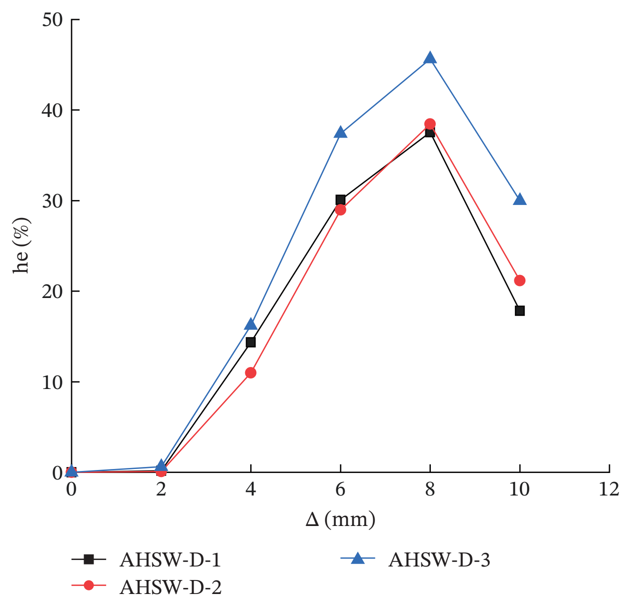

FIGURE 21 | Equivalent viscous damping coefficients of specimens AHSW-D-1–3.

TABLE 16 | Displacement angles of specimens AHSW-D-1–3.

	Yield		Peak value		Limit		
Specimen number	**Displacement (mm)**	**Displacement angle (rad)**	**Displacement (mm)**	**Displacement angle (rad)**	**Displacement (mm)**	**Displacement angle (rad)**	**Ductility coefficient**
AHSW-D-1	2.84	1/873.24	10.74	1/230.92	4.61	1/537.70	1.63
AHSW-D-2	2.85	1/870.18	10.79	1/229.84	5.74	1/432.26	2.01
AHSW-D-3	2.82	1/879.43	10.72	1/231.34	5.40	1/459.26	1.91

importance of balanced dimensions for favorable structural outcomes. From the hysteresis curves, it can be seen that the hysteresis loop areas of the three are basically the same, showing similar deformation and energy dissipation capabilities.

5.3.2 | Lateral Stiffness and Ductility

Figure 20 indicates that as the steel box dimensions increase, initial stiffness declines. Specimen AHSW-D-2 demonstrates effective seismic energy dissipation with minimal stiffness degradation, ensuring structural stability under sustained loading. Table 16 reveals that AHSW-D-3 exhibits a smaller yield displacement angle.

5.3.3 | Energy Dissipation Capacity

Figure 21 illustrates that the viscous damping coefficient decreases at the ultimate load, indicating reduced seismic resistance. Specimen AHSW-D-1 achieves the best damping performance among the three.

6 | Conclusions

This study proposes a joint connection mode for prefabricated hollow slab walls. The reliability of the joint connection was verified through comparative analysis with current engineering practices. The findings are summarized as follows:

1. Among the three dimensions studied in this paper, the 165 mm × 165 mm × 120 mm steel box exhibits the optimal balance of load-bearing capacity, stiffness, and ductility, making it the recommended size.
2. Aspect ratio: Aspect ratio significantly influences seismic performance. Higher ratios reduce the yield load and bearing capacity but increase ductility. A wall height of 2480 mm, corresponding to an aspect ratio of 2.07, is recommended as an engineering reference.
3. Axial compressive force ratios: Structural performance improves as the ratio of axial compressive force to ultimate capacity increases up to 0.3, after which performance declines. A ratio of 0.3 is recommended for practical engineering applications, balancing ductility and bearing capacity. This joint connection mode enhances structural integrity, construction efficiency, and seismic performance, making it a viable solution for prefabricated hollow slab wall systems. In the future, these vertical load-bearing hollow wall panels may be used in low-to-mid-rise prefabricated buildings (e.g., 6–8 stories or less). For taller structures or regions with different seismic fortification intensities, a more detailed analysis is required.

Future research will conduct static tests on the entire wall structure. Additionally, for the simplified treatment of bolt connections in the finite element modeling, subsequent studies will consider the bond-slip effect and establish a more refined contact model to enhance the accuracy of numerical simulations. Furthermore, the steel box construction will be optimized based on experimental results, and this joint configuration will be extended to multistory structural systems for seismic analysis, thereby further verifying its applicability and reliability under a broader range of engineering conditions.

Acknowledgments

This work was supported by the National Natural Science Foundation of China Youth Science Foundation Project (Grant 52108207), the Key Scientific Research Projects of Colleges and Universities in Henan Province (Grant 24A560002), and the Science and Technology Tackling Project of Henan Provincial Department of Education (Grant 252102320296).

Funding

This work was supported by the National Outstanding Youth Science Fund Project of National Natural Science Foundation of China (Grant 52108207), the Key Scientific Research Projects of Colleges and Universities in Henan Province (Grant 24A560002), and the Science and Technology Tackling Project of Henan Provincial Department of Education (Grant 252102320296).

Conflicts of Interest

The authors declare no conflicts of interest.

Data Availability Statement

The data that support the findings of this study are available upon request from the corresponding author. The data are not publicly available due to privacy or ethical restrictions.

References

1. M. Wasim, P. Vaz Serra, and T. D. Ngo, “Design for Manufacturing and Assembly for Sustainable, Quick and Cost-Effective Prefabricated Construction—A Review,” *International Journal of Construction Management* 22, no. 15 (2022): 3014–3022.

2. L.-K. Chen, R.-P. Yuan, X.-J. Ji, et al., “Modular Composite Building in Urgent Emergency Engineering Projects: A Case Study of Accelerated Design and Construction of Wuhan Thunder God Mountain/Leishenshan Hospital to COVID-19 Pandemic,” *Automation in Construction* 124 (2021): 103555.

3. M. Rettinger, G. Moser, N. Frank, et al., “Design for Manufacturing and Assembly as a Design Principle for Modular Precast Concrete Construction: Application Examples From the DFG Priority Programme 2187,” *Bautechnik* 102, no. 8 (2025): 458–470.

4. S. Gao, R. Jin, and W. Lu, “Design for Manufacture and Assembly in Construction: A Review,” *Building Research & Information* 48, no. 5 (2020): 538–550.

5. General Office of the State Council, “Opinions on Promoting Green Development of Urban and Rural Construction,” (2021).

6. T. Meng, “Experimental and Theoretical Research on Seismic Performance of Precast Concrete Hollow Core Wall Panels,” (Beijing Institute of Technology, 2009).

7. Y. Leigang, “Research on Seismic Performance of Precast Concrete Hollow Core Slab Shear Wall,” (Beijing Institute of Technology, 2017).

8. H. C. Chen, J. L. Liang, and M. C. Jin, “Research on Performance of Precast Two-Way Hollow Slab Shear Wall With Cast-In Situ Boundary Elements,” *Applied Mechanics and Materials* 477–478 (2013): 655–659.

9. W. Zhang, L. Yang, X. Guo, A. Li, J. Qian, and Y. Zhang, “Experimental and Numerical Study on Seismic Performance of Precast Concrete Hollow Shear Walls,” *Engineering Structures* 291 (2023): 116170.

10. H.-K. Choi, Y.-C. Choi, and C.-S. Choi, “Development and Testing of Precast Concrete Beam-to-Column Connections,” *Engineering Structures* 56 (2013): 1820–1835.

11. S. Singhal, A. Chourasia, S. Chellappa, and J. Parashar, “Precast Reinforced Concrete Shear Walls: State of the Art Review,” *Structural Concrete* 20, no. 3 (2019): 886–898.

12. D.-H. Qiao, Y.-Q. Xu, X. Zhang, J.-B. Pang, K. Liu, and S.-J. Wang, “Seismic Behaviour and Size Effect of Column Base Joints With Inverted Exposed Grouted Sleeves,” *Journal of Building Engineering* 51 (2022): 104333.

13. P. Seiff, R. S. Henry, and J. M. Ingham, “In-Plane Cyclic Testing of Precast Concrete Wall Panels With Grouted Metal Duct Base Connections,” *Engineering Structures* 184 (2019): 85–98.

14. W.-B. Ni, D.-H. Qiao, H.-W. Sun, X. Zhang, Z.-W. Zhang, and S.-J. Wang, “Seismic Performance of a Full-Scale Precast Concrete L-Shaped Column Frame Structure With a Grouted Connection,” *KSCE Journal of Civil Engineering* 26, no. 2 (2022): 753–769.

15. L. Hofer, M. A. Zanini, F. Faleschini, and K. Toska, “Seismic Behavior of Precast Reinforced Concrete Column-to-Foundation Grouted Duct Connections,” *Bulletin of Earthquake Engineering* 19, no. 12 (2021): 5191–5218.

16. R. Pramodh, V. Shripriyadharshini, and R. Vidjeapriya, “Shear Behavior of Horizontal Joints Between Precast Panels,” *Asian Journal of Civil Engineering* 19, no. 6 (2018): 651–662.

17. H. Jiang, Z. Chen, Z. Fang, et al., “Rapid Hardening High Performance Concrete (RHHPC) for Bridge Expansion Joints: From Material Properties to Interfacial Shear Performance,” *Construction and Building Materials* 458 (2025): 139638.

18. S. Zou, R. Chen, H. Wang, Z. Fang, C. Qu, and C. Zhang, “Effect of Shear Key Geometrical Dimensions on Seismic Performance of Prefabricated Concrete Piers With Shallow Socket Connections,” *Structures* 71 (2025): 107975.

19. S. Zou, H. Wang, S. Fang, et al., “Seismic Isolation Effect and Parametric Analysis of Simply Supported Beam Bridges With Multi-Level Sliding Friction Adaptive Isolation Bearing,” *Soil Dynamics and Earthquake Engineering* 188 (2025): 109000.

20. S. Dires and T. Tannert, “Performance of Coupled CLT Shear Walls With Internal Perforated Steel Plates as Vertical Joints and Hold-Downs,” *Construction and Building Materials* 346 (2022): 128389.

21. J. Jiang, J. Luo, W. Xue, X. Hu, and D. Qin, “Experimental Study on Hysteresis Behavior of Precast Concrete Double Skin Shear Wall With Horizontal Loop Connection and Spiral-Conffned Vertical Lap Connection,” *Journal of Building Engineering* 45 (2022): 103526.

22. Q. Fu, Z.-W. Cao, X.-D. Liao, Y.-N. Liu, and S.-Q. Zhang, “Quasi-Static Test and Simpliffed Analysis Method of a New Type Precast Shear Wall With Unconnected Vertical Distributed Reinforcements,” *Journal of Building Engineering* 47 (2022): 103794.

23. X. Liao, S. Zhang, Z. Cao, and X. Xiao, “Seismic Performance of a New Type of Precast Shear Walls With Non-Connected Vertical Distributed Reinforcement,” *Journal of Building Engineering* 44 (2021): 103219.

24. A. W. Abbood, K. M. Al-Obaidi, H. Awang, and A. M. Abdul Rahman, “Achieving Energy Efffciency Through Industrialized Building System for Residential Buildings in Iraq,” *International Journal of Sustainable Built Environment* 4, no. 1 (2015): 78–90.

25. Y. Chen, K. E. Galal, and A. K. Athienitis, “Integrating Hollow-Core Masonry Walls and Precast Concrete Slabs Into Building Space Heating and Cooling,” *Journal of Building Engineering* 5 (2016): 277–287.

26. X. Zhang, X. Liu, Z. Lu, and J. Xu, “Experimental Study on Seismic Performance of Precast Hollow Shear Walls,” *The Structural Design of Tall and Special Buildings* 30, no. 9 (2021): e1856.

27. N. H. Hamid and J. B. Mander, “Lateral Seismic Performance of Multipanel Precast Hollowcore Walls,” *Journal of Structural Engineering* 136, no. 7 (2010): 795–804.

28. Y. Wang, Y. Li, S. Qu, B. Cai, and C. Yan, “Seismic Performance of Prefabricated Hollow Core Slab Walls With Horizontally Connected Embedded Steel Frames,” *AIP Advances* 15, no. 4 (2025): 045225.

29. Y. Li, Z. Li, Z. Tang, et al., “Cyclic Behavior of Hollow-Core Precast Shear Walls Subjected to Different Axial Loads,” *Engineering Structures* 276 (2023): 115343.

30. GB 50010-2010, “Code for Design of Concrete Structures (in Chinese),” (China Architecture & Building Press, 2010).

31. GB 50017-2017, “Code for Design of Steel Structures (in Chinese),” (China Architecture & Building Press, 2017).

32. JGJ 101-2015, “Specification for Seismic Test of Buildings (in Chinese),” (China Architecture & Building Press, 2015).

33. ACI318-08, Standard, “Building Code Requlrements for Structure Concrete and Commentary,” (American Concrete Institute, 2008).